mater.scichina.com link.springer.com

Sci China Mater 2026, 69(2): 1223–1228
https://doi.org/10.1007/s40843-025-3764-5

Vacancy-engineered high-conductivity chloride solid-state electrolytes for long-life all-solid-state batteries

Guangwen Zhang[1†], Deyuan Li[1†], Can Xiao[1†], Huilin Ge[1], Juan Du[2], Aibing Chen[2*] and Chunpeng Yang[1*]

Rechargeable lithium-ion batteries (LIBs) have been widely used in portable electronics and electric vehicles, and are increasingly applied for grid-scale renewable energy integration [1–3]. However, conventional LIBs typically employ flammable liquid electrolytes, which not only pose serious safety hazards but also limit their energy density, hindering their broader adoption in emerging fields, such as intelligent transportation and low-altitude aviation [4]. Compared to conventional LIBs, all-solid-state batteries (ASSBs) with solid-state electrolytes (SSEs) exhibit enhanced safety, higher energy density, and longer cycle life, representing a next-generation alternative [5–8]. The performance of ASSBs is largely dictated by the properties of the SSEs [9,10]. In recent years, with the continuous deepening of understanding regarding ionic migration mechanisms, the ionic conductivity of SSEs has achieved significant improvement [11,12]. Among the diverse SSEs under active development, sulfide SSEs have attracted extensive attention due to their exceptional ionic conductivity (up to 10^{-2} S cm^{-1}) at room temperature. However, practical application of sulfide SSEs is hindered by extreme moisture sensitivity and compatibility issues with high-voltage cathodes [13,14]. In contrast, oxide SSEs offer better electrochemical and chemical stability, but suffer from poor contact with electrodes, which often results in high interfacial resistance. Recently, metal chloride SSEs (Li_aMCl_b, M = In, Y, Er, etc.), with high ionic conductivity, mechanical deformability, and excellent compatibility with high-voltage cathodes, have emerged as promising candidates for high-energy and long-life ASSBs [15–17].

However, the ionic conductivity and anode stability of chloride SSEs need to be further improved to meet the stringent requirements of practical ASSBs applications. In the past decade, a wide range of chloride SSEs, particularly those based on the Li_3ScCl_6 [18], $Li_{2.73}Ho_{1.09}Cl_6$ [19], and Li_3InCl_6 (LIC) [20] systems, have been reported with room-temperature ionic conductivities on the order of 10^{-3} S cm^{-1}. Researchers have adopted aliovalent doping strategies, substituting trivalent center metal ions with tetravalent metal ions, such as Zr^{4+} or Hf^{4+}, to engineer lattice defects, modulate Li^+ vacancy content, and further enhance ionic conductivities [21–26]. However, research on the doping of pentavalent metal ions within chloride SSEs remains relatively scarce. The impact of pentavalent metal ions on electrolyte structure and ionic transport properties requires further investigation and explanation. Based on the principle of charge compensation, each pentavalent ion substituting for a trivalent center metal ion should theoretically induce the formation of two Li^+ vacancies in the anion lattice, exhibiting twice the theoretical vacancy generation efficiency compared with doping using tetravalent ions.

In this study, we designed a range of $Li_{3-2x}In_{1-x}Ta_xCl_6$ (LITxC, $0 \leqslant x \leqslant 0.6$) by introducing Ta^{5+} as a dopant in chloride SSE—LIC, systematically exploring the influence of pentavalent doping in the cubic close packing (ccp) structure. Our findings demonstrate that Ta^{5+} incorporation efficiently increases the Li^+ vacancy content without disrupting the original crystal structure, and illustrates the relationship between Li^+ vacancy content and Li^+ transport under different scenarios. Notably, $Li_{2.4}In_{0.7}Ta_{0.3}Cl_6$ (LIT0.3C) achieves an optimal ionic conductivity of 2.19 mS cm^{-1} at 30 °C and a low Li^+ migration activation energy of 0.273 eV, which achieves an approximate balance between Li^+ vacancy concentration and Li^+ content. Meanwhile, the Ta^{5+}-doping can enhance the kinetic stability against the anode of LIT0.3C. As a result, ASSBs with LIT0.3C deliver remarkable capacity and cycling stability (500 cycles with 84.1% capacity retention at 0.2 C and 1000 cycles with 80.7% capacity retention at 0.5 C). Pentavalent Ta^{5+}-doping can optimize the ionic conductivities of chloride SSEs, with additional enhancement of anode stability, highlighting its significant application potential in high-performance ASSBs.

To explore the effect of vacancy engineering on ionic transport of SSEs, we synthesized a series of Ta^{5+}-substituted LIC (LITxC) by ball milling. X-ray diffraction (XRD) measurements were conducted to investigate the structure of the samples. The ball-milled LITxC (B-LITxC) shows broad and weak XRD peaks due to low crystallinity (Fig. S1). To enhance crystallinity and improve Li^+ transport, the B-LITxC samples were annealed at 260 °C for 5 h. After annealing treatment, the XRD patterns show significantly sharpened and intensified peaks (Fig. 1a), indicating enhanced crystallinity. XRD patterns of both B-LITxC and LITxC confirm that the original crystal structure of the undoped phase (*C2/m* space group, ICDD No. 04-09-9027) was retained across all doping levels, demonstrating that Ta^{5+} substitution did not induce phase transformation. Meanwhile, a systematic shift toward a higher angle of the main diffraction peaks (2θ = 49.3°) corresponding to the (060) crystal plane is

[1] Tianjin Key Laboratory of Advanced Carbon and Electrochemical Energy Storage, School of Chemical Engineering and Technology, National Industry-Education Integration Platform of Energy Storage, and Collaborative Innovation Center of Chemical Science and Engineering (Tianjin), Tianjin University, Tianjin 300350, China
[2] College of Chemical and Pharmaceutical Engineering, Hebei University of Science and Technology, Shijiazhuang 050018, China
† Equally contributed to this work.
* Corresponding author (email: chen_ab@163.com; cpyang@tju.edu.cn)

© Science China Press 2025

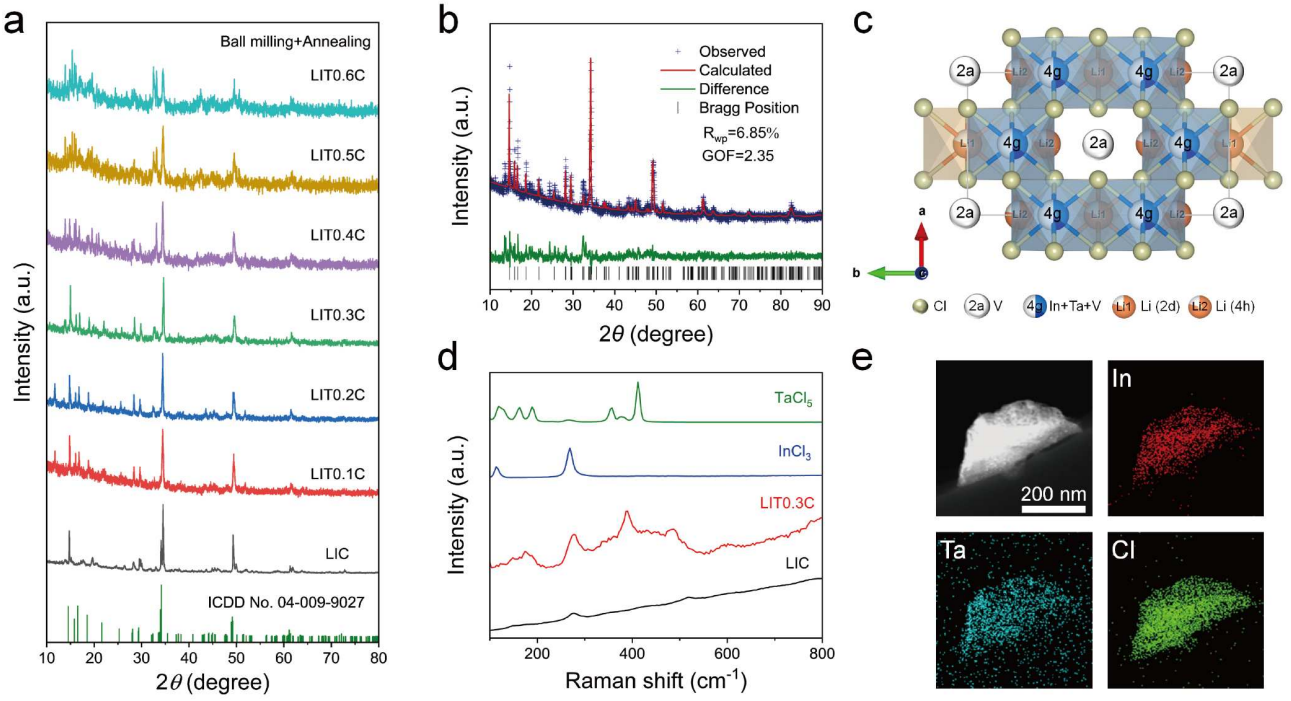


Figure 1 Structure of LIT*x*C. (a) XRD profiles of LIT*x*C. (b) XRD Rietveld refinement plots of LIT0.3C. (c) Graphical representation of the LIT0.3C unit cell (from Rietveld refinement) viewed along the *c*-axis. (d) Raman spectra of the samples. (e) EDS mapping images of elemental distribution in a LIT0.3C particle.

observed with increasing Ta^{5+} content (Fig. S2), which can be attributed to lattice contraction due to Ta^{5+}-substitution for larger In^{3+} ($r_{Ta^{5+}}$ = 0.64 Å, $r_{In^{3+}}$ = 0.8 Å) [27]. Rietveld refinement results of LIT0.3C were indexed to LIC (ICDD No. 04-09-9027), indicating that the sample retains monoclinic symmetry in structure (Fig. 1b, Fig. S3, and Table S1). The lattice parameters decrease to a = 6.417 Å, b = 11.086 Å, c = 6.382 Å, with α = 90°, β = 109.85°, and γ = 90°, subsequently resulting in a smaller unit cell volume (427.0 $Å^3$), which further indicates that the incorporation of Ta^{5+} with a smaller ionic radius leads to lattice shrinkage. Here, the graphical representation of the LIT0.3C unit cell (from Rietveld refinement) (Fig. 1c) exhibits the creation of Li^+ vacancies, occupying the octahedral central sites (2d and 4h). Based on the principle of charge compensation, each Ta^{5+} substituting for an In^{3+} should theoretically induce the formation of two Li^+ vacancies in the anion lattice. Meanwhile, the high-valent cationic distribution differs from that of LIC (ICDD No. 04-09-9027). Instead of most of In^{3+} occupying the 2a octahedral sites in LIC, both In^{3+} and Ta^{5+} occupy the 4g octahedral sites in LIT0.3C, leading to the induction of additional vacancies at the 2a sites. The vacancies at the 4g sites, which are shared with In^{3+} and Ta^{5+}, exhibit an occupancy rate of approximately 50%. In contrast, the vacancies at the 2a sites show a 100% occupancy rate [28,29].

Raman spectra (Fig. 1d) show that LIT0.3C retains the characteristic peak (around 270 cm^{-1}) related to LIC phase [30]. Meanwhile, with the doping of Ta^{5+}, the characteristic peak exhibits a blue shift compared with the pristine LIC and there are extra peaks (around 400 cm^{-1}) in LIT0.3C. Energy dispersive spectroscopy (EDS) mapping images of elemental distribution in a LIT0.3C particle show the homogeneous distribution of each element in the particle without discernible phase separation or agglomeration (Fig. 1e), confirming that Ta^{5+} has successfully and uniformly substituted. Based on the integrated analyses of XRD, Raman spectroscopy, and EDS mapping, we confirmed the successful synthesis of Ta^{5+}-substituted LIT*x*C with *C2/m* space group.

To investigate the Li^+ transport property of the samples, we conducted electrochemical impedance spectroscopy (EIS) measurements of the samples. EIS plots (Fig. 2a and Fig. S4) show that LIT0.3C exhibits the highest ionic conductivity of 2.19 mS cm^{-1} after annealing at 260 °C for 5 h, which shows a significant improvement compared to that of LIC (1.02 mS cm^{-1}). The LIT0.3C exhibits similar properties to LIC as reported in the literature [20], whereas higher annealing temperatures or longer sintering times are not optimal to achieve a structure with a high ionic conductivity (Fig. S5). Temperature-dependent EIS measurements of LIT*x*C were performed over the temperature range of 30–80 °C (Fig. 2b and Fig. S6) to determine the Li^+ migration activation energies (E_a). The results indicate that LIT0.3C exhibits the lowest E_a of 0.273 eV, lower than that of pristine LIC (0.337 eV). We further investigated the effect of Li^+ vacancy concentration on ionic conductivity. The Li^+ vacancy contents were calculated under different Ta^{5+} doping contents (x in LIT*x*C), while simultaneously correlated with Li^+ content, ionic conductivity, and Li^+ migration activation energy (Tables S2 and S3). Fig. 2c shows that, with the increase of Ta^{5+}-doping content, the ionic conductivities of LIT*x*C exhibit a trend of first increasing and then decreasing at high Ta^{5+}-doping levels, reaching the highest value of 2.19 mS cm^{-1} when x = 0.3. At this point, the theoretical Li^+ vacancy concentration is an intermediate level of 0.43, achieving an approximate balance between Li^+ vacancy concentration and Li^+ content. In contrast, E_a of LIT*x*C shows an opposite trend, first decreasing and then increasing, with the lowest E_a of 0.273 eV of LIT0.3C. Compared with the metal halide SSEs

© Science China Press 2025

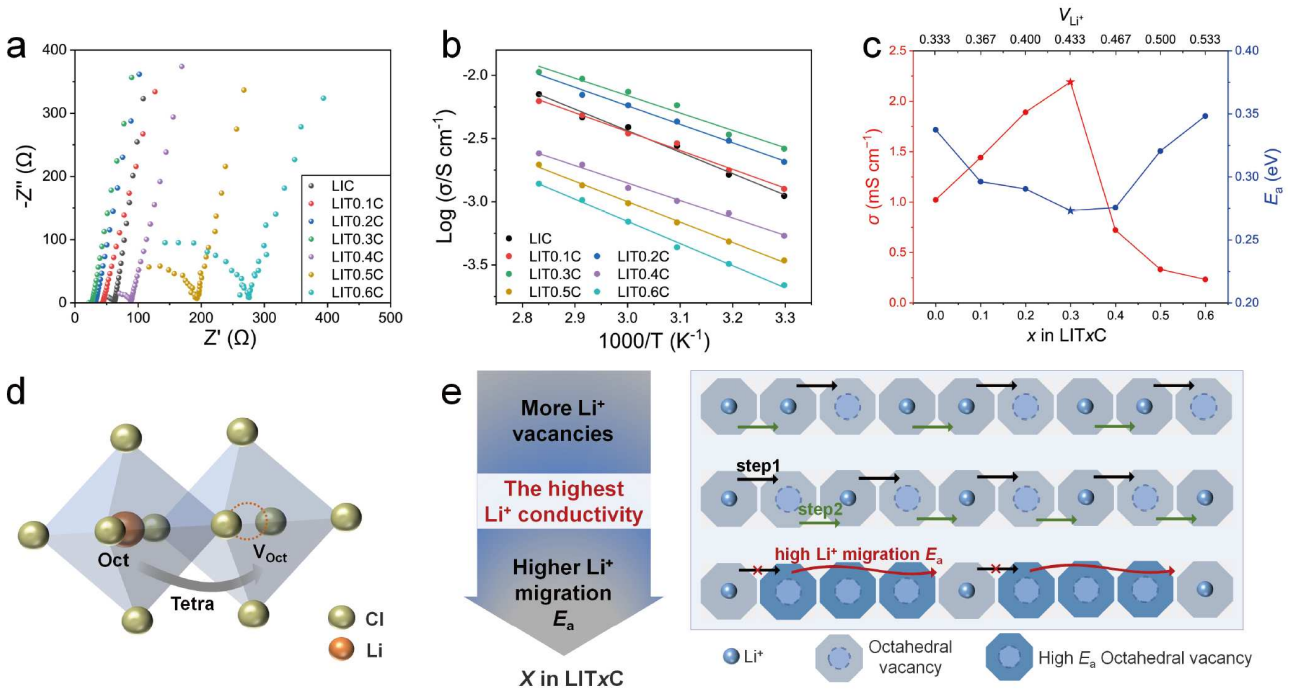


Figure 2 Ionic conductivity analyses. (a) Nyquist plots of the EIS results for LIT*x*C and LIC. (b) Arrhenius plots of LIT*x*C and LIC. (c) Plots of ionic conductivity and Li^+ migration activation energy as a function of Li^+ vacancy content and variable *x* in LIT*x*C. (d) Li^+ conduction pathway in the ccp anion structure (octahedral-tetrahedral-octahedral pathway). (e) Diagram of different transport pathways with various Li^+ contents in LIT*x*C.

reported in the literature (Table S4), Ta-doped LIT0.3C delivers a high ionic conductivity and low activation energy.

Li^+ conducts through an octahedral-tetrahedral-octahedral pathway in all directions with a 3D isotropic network within the anion framework (Fig. 2d) [31]. Based on the principle of charge compensation, the substitution of In^{3+} by pentavalent Ta^{5+} induces the generation of additional octahedral vacancies, increasing the Li^+ vacancy content from 0.333 to 0.533, which doubles the increase of Li^+ vacancy content achieved by tetravalent ion substitution (from 0.333 to 0.433). We propose the different scenarios of Li^+ migration under various Li^+ vacancy content, investigating the Li^+ transport behavior (Fig. 2e). At low doping levels, the creation of Li^+ vacancies enhances ionic mobility by providing more accessible hopping sites. However, the formation of excessive vacancies at high doping concentrations increases the energy of transition states, preventing Li^+ from forming continuous and effective ionic transport pathways, and restricting Li^+ migration, with an increase in activation energy and a decline in ionic conductivity. When the doping ratio is x = 0.3 and Li^+ vacancy content is 0.433, the ionic conductivity of LIT0.3C reaches a maximum of 2.19 mS cm^{-1}, corresponding to the lowest E_a of 0.273 eV. The enhanced ionic conductivity originates from vacancy-assisted Li^+ transport, which optimizes carrier concentration, improves diffusion pathway connectivity, and lowers migration barriers [32–34]. Meanwhile, the electronic conductivity of LIT0.3C is 2.13 × 10^{-9} S cm^{-1} (Fig. S7).

To evaluate the effect of Ta^{5+} doping on the interfacial stability against the anode, we fabricated symmetric cells with the configuration of LiIn|LIT*x*C|LiIn (Fig. 3a). The cycling performance of samples with different Ta^{5+} doping ratios was systematically compared. Fig. 3b shows that the cycling stability of symmetric cells gradually improves with the increase in Ta^{5+} doping ratio. Specifically, the symmetric cell with LIT0.6C exhibits a low polarization voltage and long cycling performance, indicating superior interfacial compatibility against the anode. In contrast, the symmetric cell with the undoped sample LIC shows a sharp voltage increase within 6 h (Fig. 3c), suggesting severe side reactions and rapid growth of interfacial resistance inside. Compared to the symmetric cell with LIC, both cells with Ta^{5+}-doped LIT*x*C (x = 0.3, 0.6) demonstrated superior cycling stability, maintaining a relatively low voltage (Fig. 3d, e). Ta^{5+} possesses a lower electronegativity and a more negative standard reduction potential than In^{3+} (Table S5), which helps suppress the reductive decomposition of the electrolyte and thereby enhances kinetic stability at the anode interface. Although Ta^{5+} doping enhances the anode stability of LIT*x*C, the material still exhibits certain interfacial resistance. Thus, a buffer layer (Li_6PS_5Cl) is required to achieve long-term compatibility in practical ASSBs [28,35]. We further conducted linear sweep voltammetry (LSV) tests to analyze the high-voltage stability of LIT0.3C. LIT0.3C delivers a higher oxidation potential (4.38 V) compared with LIC (4.25 V) (Fig. S8), confirming its enhanced high-voltage stability. Ta^{5+} doping enhances electrolyte stability by forming strong Ta–Cl bonds that reinforce the structural stabilization, while its low electronegativity improves the kinetic stability against the anode [36].

To assess the practical applicability of LIT0.3C, we performed electrochemical performance analyses on ASSBs with Ni90 ($LiNi_{0.9}Co_{0.05}Mn_{0.05}O_2$) and NCM523 ($LiNi_{0.5}Co_{0.2}Mn_{0.3}O_2$) cathodes. We first performed the electrochemical test of the Ni90 ASSBs. To compare the stability and evolution of voltage and capacity, we performed differential capacity over voltage (dQ/dV) analyses for ASSBs with LIT0.3C and LIC (Fig. 4a and Fig. S9). In the dQ/dV curves, the H2-H3 phase transition peak at 4.1 V is typically associated with irreversible *c*-axis lattice

© Science China Press 2025

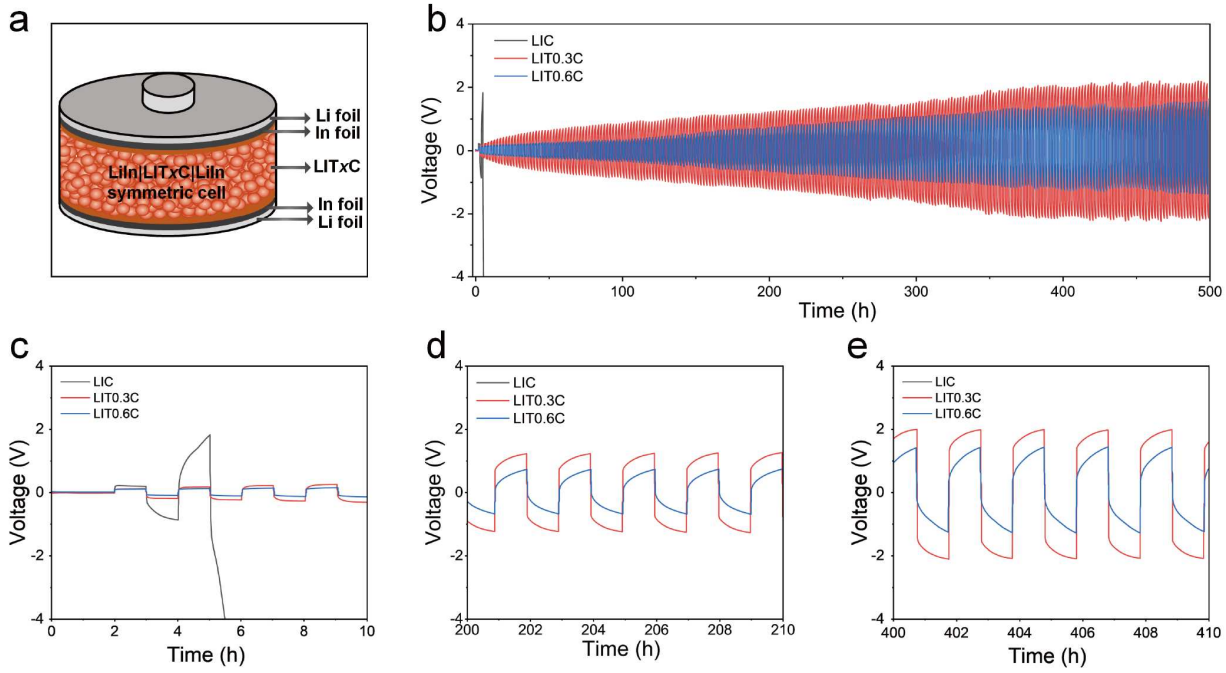


Figure 3 Anode stability performances. (a) Schematic diagram of symmetric cells in this work. (b) Cycling performance of the LiIn|LIT*x*C|LiIn symmetric cells. Enlarged views of LiIn|LIT*x*C|LiIn cells cycle curve of the (c) 0–10 h, (d) 200–210 h, and (e) 400–410 h.

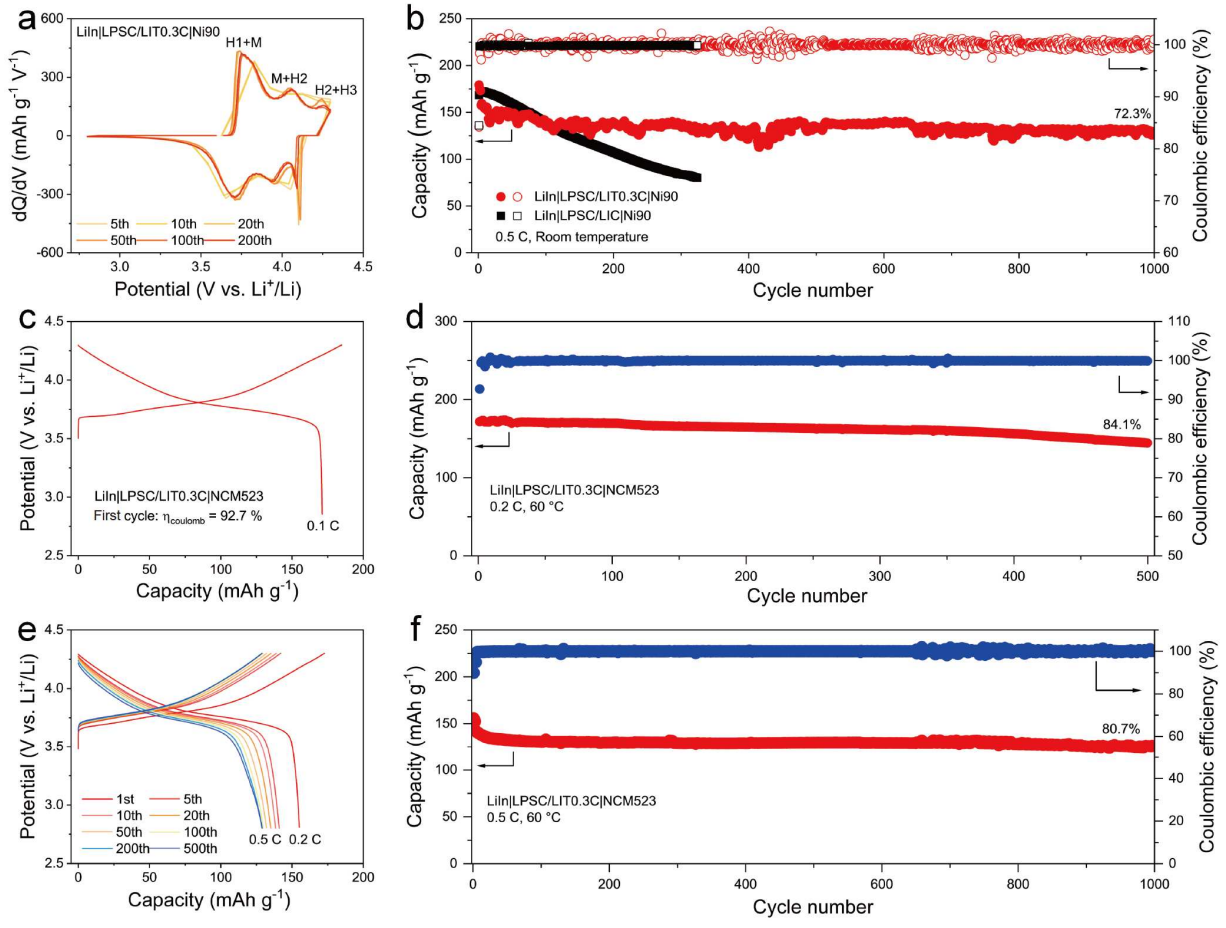


Figure 4 Long-term cyclic performance of ASSBs. (a) d*Q*/d*V* curves of the Ni90 ASSB with LIT0.3C. (b) Cycling performance of the Ni90 ASSBs with LIT0.3C and LIC at 0.5 C. (c) Initial charge-discharge curves of the NCM523 ASSB with LIT0.3C at 60 °C and (d) corresponding cycling performance. (e) Typical charge-discharge curves of the NCM523 ASSB with LIT0.3C at 60 °C, 0.5 C, and (f) corresponding cycling performance.

© Science China Press 2025

distortion in high-nickel cathode materials, which can reflect the reversibility of ASSBs [37]. Compared to the ASSB with LIC, the one with LIT0.3C shows less voltage and capacity fading, suggesting improved reversibility by suppressing the irreversible H3 phase transformation. Ni90 ASSB with LIT0.3C (Fig. 4b and Fig. S10) maintains 72.3% capacity retention after 1000 cycles at 0.5 C, while ASSB with LIC exhibits a significantly faster capacity decay, with the capacity retention dropping to less than 50% after 300 cycles.

We further conducted long-term cycling tests at various rates on the NCM523 ASSB at 60 °C to verify the application potential of LIT0.3C. The NCM523 ASSB with LIT0.3C delivers an initial capacity of 171.5 mAh g^{-1} with an initial coulombic efficiency of 92.7% at 0.1 C (Fig. 4c) and retains 84.1% capacity retention after 500 cycles at 0.2 C (Fig. 4d). NCM523 ASSB with LIT0.3C delivers 80.7% capacity retention after 1000 cycles (Fig. 4e, f). The Ta^{5+}-doped LIT0.3C not only supports efficient Li^+ transport with high ionic conductivity but also maintains the high stability under practical operating conditions. The consistent performance of the ASSBs with LIT0.3C outperforms the undoped LIC system in both capacity and cycling stability across different cathode chemistries and test conditions. The LIT0.3C electrolyte exhibits high potential for practical applications, owing to a combination of its superior electrochemical performance, scalable synthesis routes, and high moisture stability [34,38].

In summary, we demonstrated that aliovalent Ta^{5+} doping effectively enhances the performance of LIC-based SSEs. By introducing pentavalent Ta^{5+} into the host lattice, we achieved controlled Li^+ vacancy generation without altering the original crystal structure (ccp). With the optimized composition, LIT0.3C exhibits a high ionic conductivity of 2.19 mS cm^{-1} and a low activation energy of 0.273 eV, suggesting that moderate Li^+ vacancy content is crucial for Li^+ migration. Ta^{5+} substitution also improves the stability against LiIn anode and high-voltage stability originating from the dual chemical and structural stabilization provided by pentavalent tantalum. Thus, ASSBs with LIT0.3C deliver excellent cycling stability under various operating conditions. These findings highlight a practical and effective strategy for improving the ionic transport and stability of chloride SSEs, providing new insights for the design of high-performance ASSBs.

Received 16 September 2025; accepted 15 October 2025; published online 23 December 2025

1 Armand M, Tarascon JM. Building better batteries. Nature, 2008, 451: 652–657
2 Chang X, Zhao YM, Yuan B, *et al.* Solid-state lithium-ion batteries for grid energy storage: opportunities and challenges. Sci China Chem, 2024, 67: 43–66
3 Etacheri V, Marom R, Elazari R, *et al.* Challenges in the development of advanced Li-ion batteries: a review. Energy Environ Sci, 2011, 4: 3243–3262
4 Janek J, Zeier WG. A solid future for battery development. Nat Energy, 2016, 1: 16141
5 Dunn B, Kamath H, Tarascon JM. Electrical energy storage for the grid: a battery of choices. Science, 2011, 334: 928–935
6 Kong J, Hou T, Shi T, *et al.* A tough, resilient, and fluorinated solid-electrolyte interphase stabilizing lithium metal in carbonate electrolytes. Sci China Mater, 2024, 67: 1403–1411
7 Wei C, Xiao Y, Wu Z, *et al.* Construction of LiCl/LiF/LiZn hybrid SEI interface achieving high-performance sulfide-based all-solid-state lithium metal batteries. Sci China Chem, 2024, 67: 1990–2001
8 Wu Z, Liu C, Jiang Z, *et al.* Enhancing solid-state lithium metal battery performance via indium-based modification of electrolytes and lithium metal surfaces: mechanistic insights and optimization. Sci China Chem, 2025, 68: 1144–1158
9 Famprikis T, Canepa P, Dawson JA, *et al.* Fundamentals of inorganic solid-state electrolytes for batteries. Nat Mater, 2019, 18: 1278–1291
10 Hu YS. Batteries: getting solid. Nat Energy, 2016, 1: 16042
11 Zhang Z, Li H, Kaup K, *et al.* Targeting superionic conductivity by turning on anion rotation at room temperature in fast ion conductors. Matter, 2020, 2: 1667–1684
12 Zhang Z, Nazar LF. Exploiting the paddle-wheel mechanism for the design of fast ion conductors. Nat Rev Mater, 2022, 7: 389–405
13 Zhu Y, He X, Mo Y. Origin of outstanding stability in the lithium solid electrolyte materials: insights from thermodynamic analyses based on first-principles calculations. ACS Appl Mater Interfaces, 2015, 7: 23685–23693
14 Zhu Y, He X, Mo Y. First principles study on electrochemical and chemical stability of solid electrolyte–electrode interfaces in all-solid-state Li-ion batteries. J Mater Chem A, 2016, 4: 3253–3266
15 Kwak H, Wang S, Park J, *et al.* Emerging halide superionic conductors for all-solid-state batteries: design, synthesis, and practical applications. ACS Energy Lett, 2022, 7: 1776–1805
16 Asano T, Sakai A, Ouchi S, *et al.* Solid halide electrolytes with high lithium-ion conductivity for application in 4 V class bulk-type all-solid-state batteries. Adv Mater, 2018, 30: 1803075
17 Wang C, Liang J, Kim JT, *et al.* Prospects of halide-based all-solid-state batteries: from material design to practical application. Sci Adv, 2022, 8: eadc9516
18 Liang J, Li X, Wang S, *et al.* Site-occupation-tuned superionic Li_xScCl_{3+x} halide solid electrolytes for all-solid-state batteries. J Am Chem Soc, 2020, 142: 7012–7022
19 Liang J, van der Maas E, Luo J, *et al.* A series of ternary metal chloride superionic conductors for high-performance all-solid-state lithium batteries. Adv Energy Mater, 2022, 12: 2103921
20 Li X, Liang J, Luo J, *et al.* Air-stable Li_3InCl_6 electrolyte with high voltage compatibility for all-solid-state batteries. Energy Environ Sci, 2019, 12: 2665–2671
21 Helm B, Schlem R, Wankmiller B, *et al.* Exploring aliovalent substitutions in the lithium halide superionic conductor $Li_{3-x}In_{1-x}Zr_xCl_6$ ($0 \leqslant x \leqslant 0.5$). Chem Mater, 2021, 33: 4773–4782
22 Kim SY, Kaup K, Park KH, *et al.* Lithium ytterbium-based halide solid electrolytes for high voltage all-solid-state batteries. ACS Mater Lett, 2021, 3: 930–938
23 Luo X, Wu X, Xiang J, *et al.* Heterovalent cation substitution to enhance the ionic conductivity of halide electrolytes. ACS Appl Mater Interfaces, 2021, 13: 47610–47618
24 Park KH, Kaup K, Assoud A, *et al.* High-voltage superionic halide solid electrolytes for all-solid-state Li-ion batteries. ACS Energy Lett, 2020, 5: 533–539
25 Wang H, Li Y, Tang Y, *et al.* Electrochemically stable $Li_{3-x}In_{1-x}Hf_xCl_6$ halide solid electrolytes for all-solid-state batteries. ACS Appl Mater Interfaces, 2023, 15: 5504–5511
26 Zhou L, Zuo T, Li C, *et al.* $Li_{3-x}Zr_x(Ho/Lu)_{1-x}Cl_6$ solid electrolytes enable ultrahigh-loading solid-state batteries with a prelithiated Si anode. ACS Energy Lett, 2023, 8: 3102–3111
27 Shannon RD. Revised effective ionic radii and systematic studies of interatomic distances in halides and chalcogenides. Acta Cryst A, 1976, 32: 751–767
28 Li X, Liang J, Chen N, *et al.* Water-mediated synthesis of a superionic halide solid electrolyte. Angew Chem Int Ed, 2019, 58: 16427–16432
29 Song Z, Wang T, Yang H, *et al.* Promoting high-voltage stability through local lattice distortion of halide solid electrolytes. Nat Commun, 2024, 15: 1481
30 Luo X, Hu X, Zhong Y, *et al.* Degradation evolution for Li_2ZrCl_6 electrolytes in humid air and enhanced air stability via effective indium substitution. Small, 2024, 20: 2306736
31 Wang S, Bai Q, Nolan AM, *et al.* Lithium chlorides and bromides as promising solid-state chemistries for fast ion conductors with good

 © Science China Press 2025

electrochemical stability. Angew Chem Int Ed, 2019, 58: 8039–8043
32 Jun KJ, Chen Y, Wei G, *et al.* Diffusion mechanisms of fast lithium-ion conductors. Nat Rev Mater, 2024, 9: 887–905
33 Schlem R, Banik A, Eckardt M, *et al.* $Na_{3-x}Er_{1-x}Zr_xCl_6$—a halide-based fast sodium-ion conductor with vacancy-driven ionic transport. ACS Appl Energy Mater, 2020, 3: 10164–10173
34 Wang K, Gu Z, Liu H, *et al.* High-humidity-tolerant chloride solid-state electrolyte for all-solid-state lithium batteries. Adv Sci, 2024, 11: e2305394
35 Wang C, Liang J, Luo J, *et al.* A universal wet-chemistry synthesis of solid-state halide electrolytes for all-solid-state lithium-metal batteries. Sci Adv, 2021, 7: eabh1896
36 Ye Y, Geng J, Zuo D, *et al.* High-voltage long-cycling all-solid-state lithium batteries with high-valent-element-doped halide electrolytes. ACS Nano, 2024, 18: 18368–18378
37 Fan X, Ou X, Zhao W, *et al. In situ* inorganic conductive network formation in high-voltage single-crystal Ni-rich cathodes. Nat Commun, 2021, 12: 5320
38 Wang S, Xu X, Cui C, *et al.* Air sensitivity and degradation evolution of halide solid state electrolytes upon exposure. Adv Funct Mater, 2022, 32: 2108805

Acknowledgement This work was supported by the National Natural Science Foundation of China (22379108 and 52202279), Tianjin Municipal Science and Technology Program (24JCZXJC00100), and Hebei Natural Science Foundation (B2024208088).

Author contributions Yang C and Chen A conceived the idea. Zhang G and Xiao C synthesized the materials and conducted the electrochemical measurements and characterizations. Zhang G, Li D, Xiao C, Ge H, and Du J performed characterizations and analyzed the data. Zhang G, Li D, and Xiao C drafted the manuscript. Yang C, Chen A, and Li D revised the manuscript. All authors contributed to the discussion of the manuscript.

Conflict of interest The authors declare that they have no conflict of interest.

Supplementary information Supplementary materials are available in the online version of the paper.



Guangwen Zhang is a Master's student enrolled in 2022 at the School of Chemical Engineering and Technology, Tianjin University, under the supervision of Prof. Chunpeng Yang. His research focuses on halide solid-state electrolytes and all-solid-state lithium metal batteries, with particular emphasis on the regulation of interfacial stability to achieve high-performance all-solid-state lithium metal batteries.



Deyuan Li is a PhD student in the School of Chemical Engineering and Technology, Tianjin University, under the supervision of Prof. Chunpeng Yang. His current research interests involve the development of new solid-state electrolytes for next-generation all-solid-state batteries with high energy density and long cycle life.



Can Xiao is an undergraduate student enrolled in 2022 at the School of Chemical Engineering and Technology, Tianjin University, supervised by Prof. Chunpeng Yang. She is engaged in research on halide solid-state electrolytes and all-solid-state lithium metal batteries.



Aibing Chen received his PhD degree in 2007 from Dalian Institute of Chemical Physics, Chinese Academy of Sciences. He is currently a professor in the College of Chemical and Pharmaceutical Engineering, Hebei University of Science and Technology. His interests concentrate on controllable preparation of porous materials, and their applications in adsorption, CO_2 capture and conversion, drug slow and controlled release, electric energy storage, and catalytic conversion.



Chunpeng Yang is a professor at Tianjin University. He received his Bachelor's degree from the University of Science and Technology of China in 2011 and his PhD degree from the University of Chinese Academy of Sciences (Institute of Chemistry) in 2016. From 2016 to 2021, he conducted postdoctoral research at the University of Maryland and joined Tianjin University in 2021. His research focuses on high-safety and high-specific-energy electrochemical energy storage.

基于空位工程的高导氯化物固态电解质助力长寿命全固态电池

章广文[1†], 李德元[1†], 肖璨[1†], 葛慧琳[1], 杜娟[2], 陈爱兵[2*], 杨春鹏[1*]

摘要 卤化物固态电解质兼具高离子电导率与良好机械柔性, 在高能量密度、长寿命全固态电池领域展现出巨大应用潜力. 本研究设计合成了$Li_{3-2x}In_{1-x}Ta_xCl_6$ ($0 \leqslant x \leqslant 0.6$)系列电解质, 通过空位工程策略调控卤化物固态电解质的离子电导率. 其中由于Ta^{5+}对锂空位浓度的调控作用, $Li_{2.4}In_{0.7}Ta_{0.3}Cl_6$在30 °C条件下离子电导率达2.19 mS cm^{-1}, 锂离子迁移活化能低至0.273 eV. 此外Ta^{5+}对In^{3+}的取代还显著提升了电解质的负极稳定性. 由$Li_{2.4}In_{0.7}Ta_{0.3}Cl_6$组装的全固态电池展现出卓越的循环性能: 在0.2 C倍率下循环500次后, 容量保持率为84.1%; 在0.5 C倍率下循环1000次后, 容量保持率仍达80.7%. 研究表明, 基于空位工程的异价离子掺杂能有效优化氯化物固态电解质的离子电导率, 为高性能全固态电池的构建提供了新策略.

 © Science China Press 2025